Rock and Soil Mechanics

Volume 42 | Issue 11 Article 3

2-23-2022

Quantitative identification of failure behaviors of 3D printed rock-like specimen containing a single hole and double cracks

Xiang-hua LIU
Faculty of Civil and Architectural Engineering, Kunming University of Science and Technology, Kunming, Yunnan 650500, China

Ke ZHANG
Faculty of Electric Power Engineering, Kunming University of Science and Technology, Kunming, Yunnan 650500, China, zhangke_csu@163.com

Na LI
Faculty of Civil and Architectural Engineering, Kunming University of Science and Technology, Kunming, Yunnan 650500, China

Fei-fei QI
Faculty of Civil and Architectural Engineering, Kunming University of Science and Technology, Kunming, Yunnan 650500, China

See next page for additional authors

Custom Citation

LIU Xiang-hua, ZHANG Ke, LI Na, QI Fei-fei, YE Jin-ming, . Quantitative identification of failure behaviors of 3D printed rock-like specimen containing a single hole and double cracks[J]. Rock and Soil Mechanics, 2021, 42(11): 3017-3028.

Quantitative identification of failure behaviors of 3D printed rock-like specimen containing a single hole and double cracks

Authors

Xiang-hua LIU, Ke ZHANG, Na LI, Fei-fei QI, and Jin-ming YE

Rock and Soil Mechanics 2021 42(11): 3017−3028 ISSN 1000−7598
https: //doi.org/10.16285/j.rsm.2021.5521 rocksoilmech.researchcommons.org/journal

Quantitative identification of failure behaviors of 3D printed rock-like specimen containing a single hole and double cracks

LIU Xiang-hua[1], ZHANG Ke[1, 2], LI Na[1], QI Fei-fei[1], YE Jin-ming[2]

1. Faculty of Civil and Architectural Engineering, Kunming University of Science and Technology, Kunming, Yunnan 650500, China
2. Faculty of Electric Power Engineering, Kunming University of Science and Technology, Kunming, Yunnan 650500, China

Abstract: In order to investigate the mechanical properties and failure mechanisms of the rock containing a single hole and double cracks, we used the 3D sand printing technique to prepare the rock-like specimens. Digital image correlation (DIC) method was employed to non-contactly monitor the deformation field of the specimens during the compression process. By calculating the convariance matrix of the horizontal, vertical and shear strains, we introduced the effective variance of the strain field to quantify and identify the failure behaviors of the specimens. The test results indicate that the mechanical properties of the standard 3D sand printed specimens are similar to those of natural sandstones, and the test data show a low dispersion. Therefore, they can be classified as a rock-like material. Due to the inclusion of the cracks, the mechanical properties of the specimens are degraded. The compressive strength and elastic modulus of the specimens each of which contains a single hole and double cracks are reduced by 8.04%–38.91% and 14.44%–27.78%, respectively, compared with those of the specimens each of which merely contains a single hole. Based on the DIC results, three basic types of cracks are identified successfully, i.e. tensile crack (Mode I), shear crack (Mode II) and mixed tensile–shear crack (Mode I–II). All the specimens each of which contains a single hole and double cracks show mixed tensile–shear failure (Mode I–II). The coalescence patterns between the hole and the cracks are influenced by their horizontal distance, and can be classified into tensile coalescence, rotation coalescence and mixed tensile–shear coalescence. The dispersion of the strain field can be quantified by the effective variance of strain field comprehensively. The effective variance of the strain field is close to zero at the initial crack closure stage and the elastic deformation stage. The cracks propagate in different manners after initiation. Based on the effective variance of the strain field, a quantitative method to identify the type of crack was proposed. The cracks can be identified as tensile crack, mixed tensile–shear crack, and shear crack, respectively, when the growth rates of the effective variance fall into the ranges of 0.72×10^{-2}–1.89×10^{-2}, 2.34×10^{-2}–3.59×10^{-2}, and 9.63×10^{-2}–32.40×10^{-2}, respectively.

Keywords: rock mechanics; hole; crack; digital image correlation (DIC) method; effective variance; crack identification

1 Introduction

Rock is naturally a complex and heterogeneous material, which contains a large number of cracks and pores developed under long-term action of geotectonic movement. These unfavorable defects can affect the mechanical properties and fracture behaviors of the rocks. Therefore, it is of paramount significance to understand the failure behaviors of rocks containing cracks and holes for ensuring the safety and stability of rock engineering.

In the past decades, numerous scholars around the world have thoroughly studied the mechanical behaviors of rocks containing internal defects. Lajtai et al.[1] firstly studied the crack propagation and interaction of gypsum specimens containing holes under compressive loading. They classified the cracks generated around the holes into three basic types: initial cracks, shear cracks, and far-field cracks. Du et al.[2] categorized the failure pattern of the rocks containing square or rhombic holes into three types: tensile failure, shear failure, and mixed tensile–shear failure. They pointed out that the structural effects induced by the internal defects can significantly affect the mechanical properties and crack propagation of the specimen. Li et al.[3] showed that the rocks containing rectangular or horseshoe-shaped holes exhibit diagonal shear failure, whereas the rocks containing circular holes exhibit X-shaped shear failure. Huang et al.[4] and Zhu et al.[5] analyzed the failure process of rocks containing elliptical holes at different inclination angles and ratios of long to short axis. They proposed a method for measuring the initial stress of rocks containing internal defects. Wong et al.[6] and Lin et al.[7] studied the impacts of the size, number and distribution of holes on the failure behaviors of rocks. It should be noted that the holes and cracks generally develop in the rock simultaneously. Yang et al.[8] conducted the uniaxial compression tests on sandstone containing holes and cracks, and concluded that the mechanical properties of the specimen are related to the geometric distribution of defects. Zhou et al.[9] numerically modeled the effect of cracks on the mechanical and failure characteristics of rocks. Wu et al.[10] combined the acoustic emission and computed tomography (CT) scanning techniques to analyze the failure process of rock specimens containing holes and cracks, and found that the interaction between holes and cracks has a significant impact on the mechanical properties and

Received: 9 April 2021 Revised: 24 August 2021
This work was supported by the National Natural Science Foundation of China (41762021, 11902128) and the Applied Basic Research Foundation of Yunnan Province (2019FI012).
First author: LIU Xiang-hua, male, born in 1994, PhD candidate, majoring in rock mechanics and engineering. E-mail: liuxianghua24@126.com
Corresponding author: ZHANG Ke, male, born in 1986, PhD, Associate, Professor, PhD supervisor, mainly engaged in teaching and research in rock mechanics and engineering. E-mail: zhangke_csu@163.com

fracture characteristics of rocks.

The 3D printing technique has the advantages of high precision and good repeatability. It has attracted increasing attention in rock mechanics discipline. This technique can be divided into stereo lithography appearance (SLA), fused deposition modeling (FDM), and selective laser sintering (SLS). Ju et al.[11] used CT scanning to accurately obtain the crack network inside the coal, and then reconstructed a specimen containing natural cracks using photosensitive resin through the SLA technique. Jiang et al.[12] found that the PLA material used in the FDM technique exhibited significant elastoplastic deformation characteristics, which is quite different from the natural rocks. Jiang et al.[13] reconstructed a physical model by 3D printing based on the 3D scanning data of the natural structural plane of the rocks, and then performed the shear tests on the cast specimens. Zhou et al.[14] prepared the standard cylindrical specimens using ceramic material and found that those specimens are incapable of simulating brittle rocks. In addition, many scholars have applied the 3D printing technique to performing the laboratory tests on rocks containing holes and defects. For instance, Jiang et al.[15] printed the specimens containing internal holes using gypsum, and pointed out that the crack propagation of gypsum specimens is similar to that of the rock, but with low uniaxial compressive strength. Wang et al.[16], Zhang et al.[17], and Jin et al.[18] printed the structural planes of different geometric shapes and roughness using the FDM technique, and then made the rock-like matrix by pouring the cement mortar. They provide a new method for preparing rock specimens containing complex fractures.

Digital image correlation (DIC) is a method that could measure the full-field rock deformation with high precision and non-contact, and it has been developed rapidly in recent years. By means of the DIC technique, Zhao et al.[19] summarized the meso-scale characteristics of the deformation and damage evolution of the rock-like materials containing a single crack. Zhou et al.[20] used DIC to observe the full-field failure behaviors of the red-bed soft rock under compressive load. Additionally, combining statistics and image processing techniques, several indicators have been proposed to quantitatively describe the development of the deformation field, such as strain localization index[21], strain field differentiation rate[22], maximum relative strain[23], correlation coefficient of image gray scale[24], and texture feature parameters of image gray scale[25]. However, these indicators are based on a certain type of the deformation field, and hard to evaluate the evolution characteristics of all the strain components.

The substrate in 3D sand printing is similar to the mineral particles and cementation components inside the natural rock. It has been applied to the field of rock mechanics in recent years. Tian et al.[26] employed this technique to prepare rock-like specimens. They found that the mechanical properties and failure characteristics of the printed specimens are more similar to those of the natural sandstones, in comparison with other types of printed specimens. Therefore, in this study, we use 3D sand printing technique to prepare the rock specimens each of which contains a single hole and double cracks. The interaction mechanism between the hole and the cracks is explored using the uniaxial compression tests. By means of the DIC technique, we quantitatively study the global strain field on the surface of the specimen from the meso-mechanics perspective. By calculating the covariance matrix of horizontal, vertical and shear strains, we propose an effective variance of the strain field, which can be used to analyze the evolution of the strain field and to identify the type of crack propagation during the loading process. The results presented in this study could gain more insights into the failure mechanism of the rock containing a single hole and double cracks.

2 Experimental programs

2.1 3D sand printing equipment and printing process

In this study, we use the new S-Max industrial 3D sand printer manufactured by Exone of Germany, as shown in Fig.1. It is a sand casting printer with a layer height of 0.26–0.38 mm and a printing accuracy of 0.1 mm. The size of the build box is 1 800 mm×1 000 mm×700 mm (length×width×height). We choose the fine-grained artificial silica sand as the printing material and the furan resin from 0.074 mm to 0.0147 mm as the binder, in order to simulate the mineral particles and cementing components inside the real rock.

Fig. 1 Printing setup

The preparation process of the specimens is described as follows. We use AutoCAD software for 3D modeling and import the *.SLT file into the printer for layering. The layer height is set to 0.3 mm. The printer lays a layer of silica sand uniformly on the printing cylinder and scrapes the surface of the silica sand with a scraper. Then the nozzle sprays a layer of furan resin on the position where needs binder. The first layer is completed, and then the working piston is lowered by one layer height. We repeat the above operations iteratively until the printing is finished. After that, we take the specimen out of the printing cylinder, remove the remaining silica sand on the surface, and place it in a room to air dry for 24 h. It should be noted that the mechanical properties of the 3D printed specimens show anisotropy as the printing direction changes. The specimens with a same structure but printed in different directions may vary considerably in the experimental results[27]. The printed specimen has an obvious layered structure, and the physical properties of each layer normal to the printing

direction show a transverse isotropy[26]. Therefore, we set the direction of printing along the *z* direction (see Fig.2), i.e. perpendicular to the loading direction, in order to eliminate the influence of anisotropy on crack propagation in the layers parallel to the *xy* plane, as well as to ensure the repeatability of the experimental results.

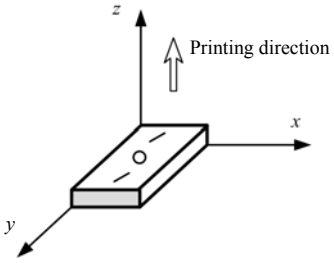

Fig. 2 Direction of 3D sand printing

2.2 Mechanical properties of 3D sand printed standard specimens

In order to study the mechanical properties of the 3D sand printed specimens, we prepare the standard cylindrical specimens with the sizes of 50 mm×100 mm (diameter×height, Nos.1–3) and 50 mm×50 mm (diameter× height, Nos.4–6) for uniaxial compression test and Brazilian splitting test, respectively. Table 1 shows the mechanical parameters of the standard cylindrical specimens. The average values of compressive strength σ_c, elastic modulus E and tensile strength σ_t are 6.12 MPa, 1.02 GPa and 0.50 MPa, respectively. The corresponding coefficients of variation are 0.039, 0.034 and 0.051, indicating that the mechanical properties of the 3D sand printed specimens are stable. The ratio of compressive to tensile strength for the specimens is 12.24:1.00, suggesting that the specimens have a good brittleness. In addition, all the mechanical parameters of the printed specimens fall within the range of those of sandstone[28] (see Table 1). Therefore, the 3D sand printed specimens could simulate sandstone properly in terms of mechanical properties and failure characteristics.

Table 1 Comparison of mechanical properties between 3D sand printed specimens and natural sandstones

Type of material	Specimen No.	Uniaxial compression test		Brazilian splitting test
		σ_c/MPa	E/GPa	σ_t/MPa
3D sand printed specimen	1	5.85	1.02	—
	2	6.31	1.05	—
	3	6.19	0.98	—
	4	—	—	0.49
	5	—	—	0.48
	6	—	—	0.53
Sandstone	—	5.11–10.06	0.75–1.39	0.10–0.88

2.3 Preparation of specimen containing a single hole and double cracks

As shown in Fig.3, the spatial distribution and geometric shape of the internal cracks and holes in the rock mass vary, which seriously affects the failure characteristics of the rock mass. Yin et al.[29] and Zhou et al.[9] comprehensively studied the effect of the vertical distance between holes and cracks on the failure characteristics of rock mass using laboratory tests and numerical simulation, respectively[9, 29]. The results show that the distance between the cracks controls the mechanical behaviors of the rock mass. The horizontal distance between the hole and the cracks is also an essential index, but it is rarely studied. Therefore, we prepare rock specimens each of which contains a single hole and double cracks through 3D sand printing, also in order to explore the effect of the aforementioned horizontal distance.

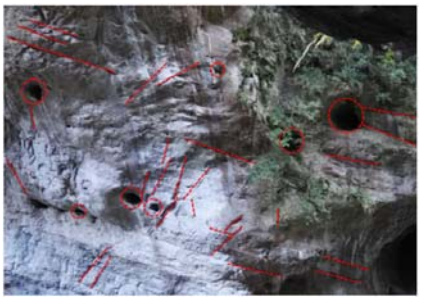

Fig. 3 Rock mass containing cracks and holes[28]

The size of the specimen containing a single hole and double cracks is designed to be 100 mm×50 mm× 20 mm (length×width×thickness). The single hole with a diameter (a) of 10 mm is located in the center of the specimen. The two prefabricated cracks (① and ②) are symmetrically distributed around the center of the specimen. The length of the crack (b) is 11.41 mm and the inclination angle (β) is 45°. The vertical distance (c) between the inner tip of the crack and the hole is 10 mm. The horizontal distances (L) between the center of the hole and the midpoint of the crack are set to be 0, 10 and 20 mm, respectively, as shown in Fig.4. For comparison, specimens each of which contains a single hole are designed. Two pieces of each type of specimen are made. The corresponding physico-mechanical parameters are shown in Table 2. The specimen No. is specified as "horizontal distance-serial number". For example, "10-1" represents the specimen #1 with a horizontal distance of 10 mm between the hole and the crack, and "N-1" represents the specimen #1 with a hole but no crack.

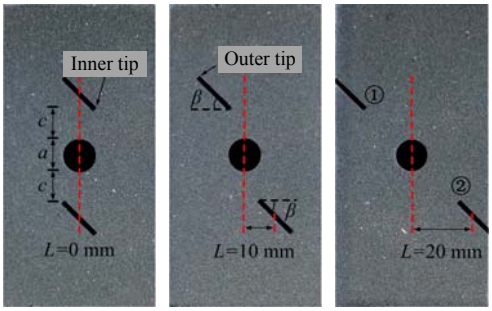

(a) L = 0 mm (b) L = 10 mm (c) L = 20 mm

Fig. 4 Geometry of specimens

Table 2 Physico-mechanical parameters of specimens each of which contains a single hole and double cracks

Specimen No.	a /mm	b /mm	c /mm	L /mm	σ_c /MPa	E /GPa
0-1	10	11.41	10	0	4.24	0.80
0-2	10	11.41	10	0	4.21	0.73
10-1	10	11.41	10	10	2.86	0.67
10-2	10	11.41	10	10	2.94	0.68
20-1	10	11.41	10	20	2.79	0.64
20-2	10	11.41	10	20	2.83	0.65
N-1	10	—	—	—	4.64	0.88
N-2	10	—	—	—	4.55	0.92

2.4 DIC method

DIC methods have the advantages of high calculation efficiency, good applicability and repeatable analysis. It can directly reflect the full-field deformation of the specimen surface during the loading process. The principle of the DIC method is described as follows. Given the digital speckle images of the specimen surface before and after the deformation, DIC chooses a certain sub-area on the image before deformation as a reference, and searches for the corresponding displacement value of speckles on the deformed image. DIC uses a correlation-based matching method to evaluate the similarity between the sub-areas and solves the corresponding displacement field. Based on this, we calculate the displacement fields of the surface of the specimen using all the speckles. Then, following Cauchy's equation, we obtain the corresponding strain field.

We make an artificial speckle field by spray painting. A layer of white paint is sprayed on the front of the specimen, and then the black paint is sprayed after drying of the white paint, so that the black paint particles can randomly fall on white paint to form a speckle field, as shown in Fig.5(a).

After the tests, we import the collected digital speckle images into a DIC data analysis software, Ncorr. Taking the digital speckle image at the initial loading stage as a reference, the deformation field of the specimen surface is calculated. In order to obtain the global displacement and strain of the specimen surface, the calculation area is usually set to cover the entire surface of the specimen[30], which is also followed in this study. For specimens with discontinuous points on the surface, the correlation-based matching method may produce large errors[31]. Therefore, our research also excludes the area of prefabricated holes and cracks. The final computational area is shown in Fig.5(b). The black area is not included in the DIC calculation.

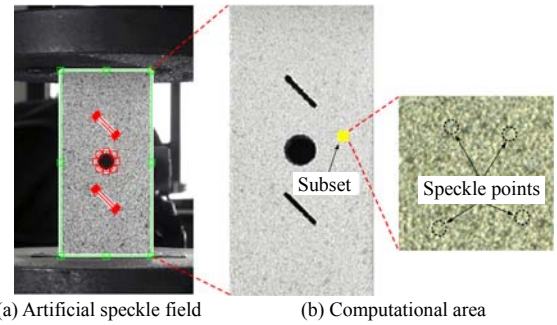

(a) Artificial speckle field (b) Computational area

Fig. 5 Computational area of DIC method

2.5 Test setup

The setup of the uniaxial compression test is shown in Fig.6. The loading equipment is the WDW-100 microcomputer-controlled universal testing machine, with a loading accuracy of 0.5%. The displacement-controlled loading method is adopted with a loading rate to 5×10^{-3} mm/s. Vaseline is daubed on the upper and lower end surfaces of the specimen to reduce the friction effect. The CCD industrial camera with resolution of 2592×1944 pixels is placed in front of the speckled surface of the specimen. LED cold light lamps are placed on both sides of the camera to provide a stable light source. According to the experience of Zhou et al.[20] and Pan et al.[32], we set the capture rate to 1 frame/s, which can capture the whole process of the crack initiation, propagation, coalescence and failure. Before the test, we synchronize the time of each device.

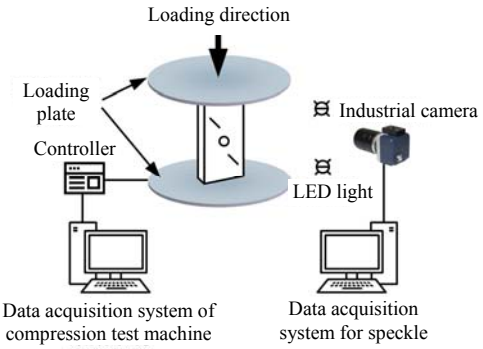

Fig. 6 Test setup

3 Test results and analysis

3.1 Strength and deformation parameters

The average value and the error bar of the mechanical parameters of the specimens each containing a single hole and double cracks are shown in Fig.7 (see Table 2 for specific values), in which σ_0 and E_0 are the average values of compressive strength and elastic modulus of the specimens each of which contains a single hole, respectively. As shown in Fig.7, the average compressive strength and elastic modulus of the specimens each of which contains a single hole are 4.60 MPa and 0.90 GPa, respectively, which are higher than those of

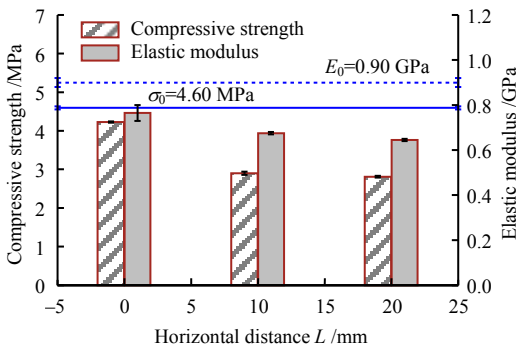

Fig. 7 Compressive strength and elastic modulus of the specimens each of which contains a single hole and double cracks

the specimens each of which contains a single hole and double cracks. It indicates that the cracks degrade the mechanical properties of rock with holes. The degradation amplitudes of compressive strength and elastic modulus range from 8.04% to 38.91%, and from 14.44% to 27.78%, respectively.

3.2 Failure pattern of specimen containing a single hole and double cracks

The failure patterns of all the specimens each of which contains a single hole and double cracks show mixed tensile–shear failure (Mode I-II). According to the fracture mechanics, three basic types of cracks are identified successfully, which are tensile crack (Mode I), shear crack (Mode II), and mixed tensile–shear crack (Mode I-II). Mode I is subjected to tensile stress perpendicular to the crack surface, Mode II is subjected to shear stress parallel to the crack surface, and Mode I-II is subjected to both tensile and shear stresses. The corresponding meso-mechanism is explained as follows. The final failure patterns of specimens are shown in Fig.8, in which "I", "II" and "I-II" represent the crack patterns, respectively.

(1) When $L=0$ mm, under the axial loading, the tensile cracks (Mode I) first appear at the upper and lower ends of the hole, and propagate approximately along the loading direction. Later, the tensile cracks also appear at the outer tips of prefabricated cracks 1 and 2 and propagate approximately perpendicular to the prefabricated cracks. As loading continues, a shear crack (Mode II) appears at the inner tip of the prefabricated crack 2 and rapidly propagate to the left boundary of the specimen. Meanwhile, the tensile cracks around the hole propagate to the middle of the prefabricated cracks. With the increase of the load on the specimen, the tensile cracks at the outer tip of cracks propagate to the upper and lower boundaries of the specimen, forming a fracture plane by linking the prefabricated cracks. Then, a shear crack appears at the inner tip of the prefabricated crack ①, and propagates to the right boundary of the specimen. In combination with the shear cracks around the prefabricated crack ②, a fracture plane is formed, and the specimen fails eventually.

(2) When $L=10$ mm, the constantly developing tensile cracks first appear around the holes and prefabricated cracks. Due to the interaction between the tensile cracks, the fragmented pieces in the specimen rotate (see the black arrows in Fig.8(b)), which in turn promotes the tensile crack propagating to the crack tip and to the both sides of the hole. As the load applied on the specimen increases, the shear cracks appear around the prefabricated crack 1, and propagate through the upper left corner to the boundary of the specimen. As the load increases continuously, the shear cracks appear at the outer tip of the prefabricated crack 2, and propagate through the lower right corner to the boundary of the specimen. In combination with the prefabricated cracks, a fracture plane is formed, and the specimen fails eventually.

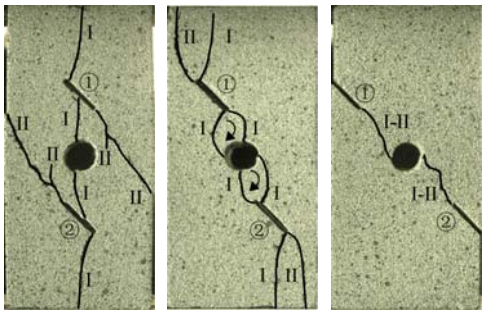

(a) 0-1 (b) 10-1 (c) 20-1

Fig. 8 Failure patterns of specimens each of which contains a single hole and double cracks

(3) When $L=20$ mm, as the external load is close to the peak stress, the mixed tensile–shear cracks (Mode I–II) appear on both sides of the hole and quickly penetrate through the rock bridge to coalesce with the prefabricated cracks. A fracture plane is formed eventually.

3.3 Failure pattern of specimen containing a single hole

The final failure pattern of the specimen containing a single hole is shown in Fig.9(a). Under the external load, the constantly developing tensile cracks appear at the upper and lower ends of the hole, but this has not resulted in the failure of the specimen. As the load on the specimen increases, the horizontal cracks appear on the left of the hole, propagating to the left boundary of the specimen. Then, the shear cracks appear on the right side of the hole and propagate through the upper and right corner, resulting in the failure of the specimen. The failure process of the specimen containing a single hole is similar to those in Yang et al.[8] (see Fig.9(b)) and Huang et al.[4] (see Fig.9(c)), indicating that the 3D sand printed specimen could be used to simulate the real sandstone.

For the specimen containing a single hole, the tensile cracks generated on both sides of the hole result in the final failure of the specimen. For the specimen containing a single hole and double cracks, the interaction between the hole and cracks changes the initiation, propagation, coalescence and failure of cracks. Initial tensile cracks will not only appear at the edge of the hole, but also at the tip of the prefabricated cracks. As the load on the specimen increases, they coalesce with the hole and the prefabricated cracks, acting as a key factor in controlling the failure of the specimen.

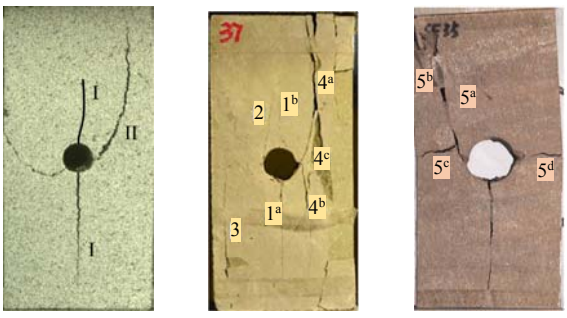

(a) N-1 (b) Test results of Yang et al.[8] (c) Test results of Huang et al.[4]

Fig. 9 Failure patterns of specimens containing only one hole

3.4 Meso-mechanism of the coalescence of hole and cracks

3.4.1 Solution of displacement vector

We use Ncorr software to calculate the horizontal and vertical displacement fields on the surface of the specimen, which yields the matrix of the displacement field. The displacement vector is solved and the displacement vector diagrams during the loading process is obtained. Let the coordinates of the points on the digital speckle image as (x, y) before deformation, and the coordinates as (x', y') after deformation, the displacement can be solved as

$$\left.\begin{aligned} l &= \sqrt{(x'-x)^2+(y'-y)^2} \\ \alpha &= \arctan\frac{\Delta y}{\Delta x} = \arctan\frac{y'-y}{x'-x} \end{aligned}\right\} \quad (1)$$

where l is the total displacement of the point to be measured; α is the angle between the displacement vector direction of the point and the horizontal direction. We assume the right direction to be positive and the left direction to be negative. Δx and Δy are the horizontal and vertical displacements of the point to be measured, respectively.

3.4.2 Calculation results and analysis

As the crack initiates, propagates and coalesces, the direction and size of the relative displacement vector of the meso-particles will change on both sides. Based on these changes, the patterns of crack propagation and the force characteristics can be identified intuitively from the perspective of meso-mechanics. Three patterns of crack propagation are identified successfully, i.e. tensile crack (Mode I), shear crack (Mode II), and mixed tensile–shear crack (Mode I-II). The calculation results of a typical displacement vector around the crack are shown in Fig.10. In order to describe the movement of meso-particles, we illustrate the overall movement trend of the particles by black hollow arrows. The length of the arrow indicates the magnitude of the displacement.

(1) Tensile crack (Mode I): The meso-particles on both sides of cracks move opposite to each other at a certain angle. The displacements of the particles are equivalent on both sides.

(2) Shear crack (Mode II): The meso-particles on both sides of cracks move in the same direction along the crack. The displacement of the particles varies greatly on both sides, showing a relative shear motion.

(3) Mixed tensile–shear crack (Mode I-II): The meso-particles on both sides of cracks move opposite to each other at a small angle. The displacements of the particles are different on both sides.

One can see from Fig.10(b), when $L = 10$ mm, the meso-particles between the hole and the cracks move clockwise, indicating the rotation of the fragmented pieces in the rock bridge area. The observation is similar to the numerical results of rock specimens with holes and cracks[33]. In combination with the diagrams of the displacement vector distribution, the rotating fragmented piece is formed by the coalescence of the tensile cracks with the hole and the prefabricated cracks, i.e. the rotating fragmented piece is mainly tensile. When the fragmented piece rotates, it increases the opening of the tensile crack. Therefore, the coalescence mode between the hole and the prefabricated cracks is rotational coalescence.

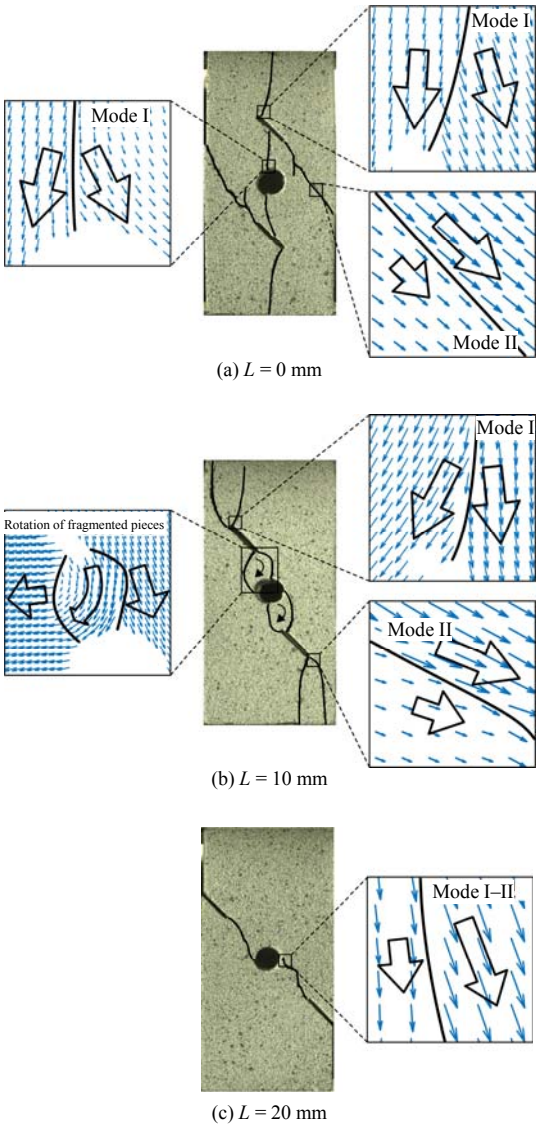

Fig. 10 Displacement vector diagrams

According to the types of cracks between holes and cracks, three patterns of coalescence can be identified: tensile coalescence, rotational coalescence, and mixed tensile–shear coalescence. The results of the specimens containing a single hole and double cracks are shown in Table 3.

Table 3 Crack types and coalescence mode between the hole and the cracks

Horizontal distance L /mm	Mode I	Mode II	Mode I-II	Coalescence mode
0	√	√	—	Tensile
10	√	√	—	Rotational
20	—	—	√	Shear

4 Quantitative analysis of failure process based on DIC and covariance matrix

4.1 Calculation principle of effective variance based on covariance matrix

Covariance matrix is an important concept in statistics and probability theory to measure the deviation of multiple components from their mean values. Its elements represent the covariance between multiple components. Gao et al.[34] proposed a metric that considers all stress components based on the covariance matrix to describe the degree of dispersion of stress data. They tested the applicability and validity of the proposed metric by in situ stress measurements. Following this method, we employ the effective variance of the strain field to study the evolution of the strain field. Then the matrix of the horizontal, vertical and shear strain field is derived, and the covariance matrix of the three strain components is calculated. We solve this matrix as a determinant and calculate its arithmetic square root, which yields the effective variance of the strain field. The detailed calculation steps are described as follows.

According to the calculation of the stress tensor in the study of Gao et al.[34], the strain tensor $\boldsymbol{S}$ can be similarly obtained as

$$\boldsymbol{S}=\begin{bmatrix}\varepsilon_{xx} & \varepsilon_{xy}\\ \text{symmetric} & \varepsilon_{yy}\end{bmatrix} \tag{2}$$

where ε_{xx}, ε_{xy} and ε_{yy} are the horizontal, shear and vertical strain fields, respectively.

The strain vector $\boldsymbol{s}_{\mathrm{d}}$ is

$$\boldsymbol{s}_{\mathrm{d}}=\mathrm{vech}(\boldsymbol{S})=\left[\varepsilon_{xx}\ \ \varepsilon_{xy}\ \ \varepsilon_{yy}\right]^{\mathrm{T}} \tag{3}$$

where vech() is the half-vectorization operator.

The covariance matrix of the three components of strain is given as

$$\boldsymbol{\Omega}=\mathrm{cov}(\boldsymbol{s}_{\mathrm{d}})=\frac{1}{n}\sum_{i=1}^{n}(\boldsymbol{s}_{\mathrm{d}_i}-\overline{\boldsymbol{s}}_{\mathrm{d}})\cdot(\boldsymbol{s}_{\mathrm{d}_i}-\overline{\boldsymbol{s}}_{\mathrm{d}})^{\mathrm{T}} \tag{4}$$

where n is the total number of the strain matrix elements; $\boldsymbol{s}_{\mathrm{d}_i}$ is the strain vector of the i-th group of the data; and $\overline{\boldsymbol{s}}_{\mathrm{d}}$ is the mean vector that obtained as

$$\overline{\boldsymbol{s}}_{\mathrm{d}}=\frac{1}{n}\sum_{i=1}^{n}\boldsymbol{s}_{\mathrm{d}_i} \tag{5}$$

The effective variance of strain field V_{e} is defined as

$$V_{\mathrm{e}}=\sqrt[\frac{1}{2}p(p+1)]{|\boldsymbol{\Omega}|} \tag{6}$$

where $|\cdot|$ is the matrix determinant; and p is the tensor dimension. In this case, strain is a two-dimensional tensor, therefore, we have $p=2$. The effective variance of the strain field can describe the deviation of the strain field during the loading process. It reflects the degree to which the strain components of the horizontal, vertical and shear fields can deviate from their mean values. The more obvious the deviation, the greater the effective variance of the strain field.

4.2 Strain distribution at the beginning of loading

Taking the calculation results of an axial strain of 0.40% as an example, we analyze the effect of the prefabricated cracks on the strain field of the specimen containing a single hole. Figure 11 shows the horizontal strain fields of specimens 0-1, 10-1, 20-1 and N-1. As shown in Figs.11(a)–11(c), for specimens each of which contains a single hole and double cracks, the high-strain area is not only distributed around the hole, but also around the tip of the prefabricated cracks. In addition, a tendency of forming a localized band of strain between the hole and the cracks can be observed. However, as shown in Fig.11(d), the values of the strain field are small for the specimen containing a single hole. In addition, the distribution of holes and cracks has the impacts on strain fields. As the horizontal distance increases, the strain field becomes more concentrated for the specimens each of which contains a single hole and double cracks, which explains the deterioration of the macroscopic mechanical parameters (see Fig.7).

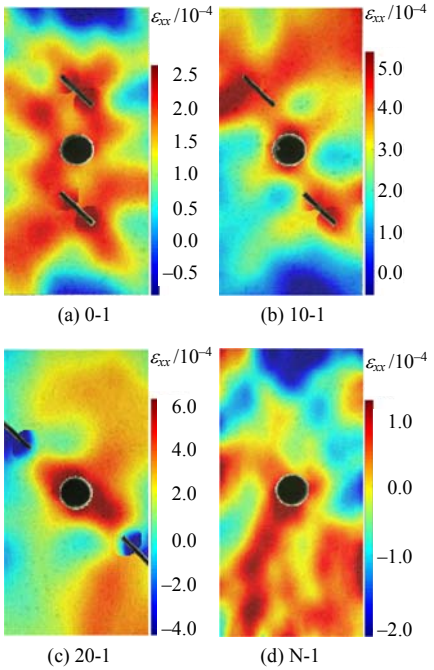

Fig. 11 Horizontal strain fields at axial strain of 0.40%

4.3 Variation of effective variance during failure process

Figures 12(a)–14(a) show the typical stress–strain curves of the specimens each of which contains a single hole and double cracks. The curves could be divided into initial compaction stage, elastic deformation stage, plastic deformation stage and the post-peak failure stage. The mark points O, A, B, C and D on the stress–strain curves correspond to different axial stress levels, and the subscripts "0", "10" and "20" represent the horizontal distance between the hole and the crack. The mark point O corresponds to the reference image, and the mark point A corresponds to the initial stage of loading (0.40% axial strain). The corresponding contours of the strain field are shown in Fig.11. Through calculating the effective variance of the strain field of the specimens

each of which contains a single hole and double cracks using Eq.(6), as shown in Figs.12(a)–14(a), the effective variance varies greatly at different stages. At the initial stage of loading, the effective variance of the strain field is close to 0, because the strain field is distributed uniformly and there is no obvious distinction. With the initiation, propagation and coalescence of cracks, the degree of dispersion of the strain field increases, resulting in a variation in the effective variance of the strain field.

(1) Figure 12 shows the stress–strain curve, effective variance, crack propagation and the horizontal strain field of the specimen 0–1 when $L=0$ mm. When loading to the mark point B_0, the tensile cracks (Mode I) initiate and a strain localization band occurs around the hole and prefabricated cracks covering the crack propagation path. The effective variance increases slowly. At the peak stress (the mark point C_0), the shear cracks (Mode II) around the prefabricated crack 2 and the corresponding strain localization band propagate to the boundary of the specimen rapidly. The deviation degree of the strain field increases suddenly, so that the effective variance increases abruptly. After that, the strain localization band have rarely changed. The strain increases, so that the effective variance increases slowly. At the axial strain of the mark point D_0, the shear cracks around the prefabricated crack 1 and the strain localization band propagate to the edge of the specimen quickly. The deviation of the strain data increases significantly, so that the effective variance also increases sharply.

(2) Figure 13 shows the stress–strain curve, effective variance, crack propagation and horizontal strain field of the specimen 10-1 when $L=10$ mm. At the axial strain of the mark point B_{10}, tensile cracks initiate around the hole and prefabricated cracks and their corresponding strain localization band grow steadily. Deviation of the strain field appears, so that the effective variance starts to grow slowly. At the peak stress (the mark point C_{10}), the shear crack at the tip of the pre-fabricated crack immediately propagates to the upper

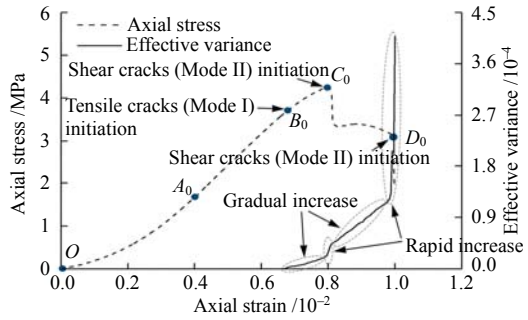

(a) Stress–strain curve

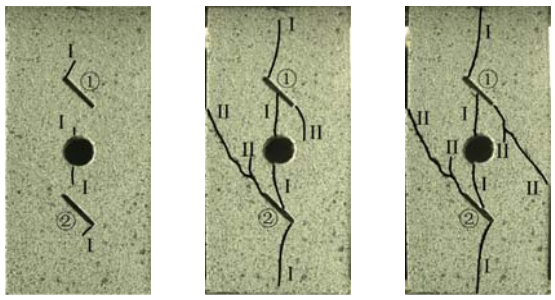

(b) Crack propagation (point B_0) (c) Crack propagation (point C_0) (d) Crack propagation (point D_0)

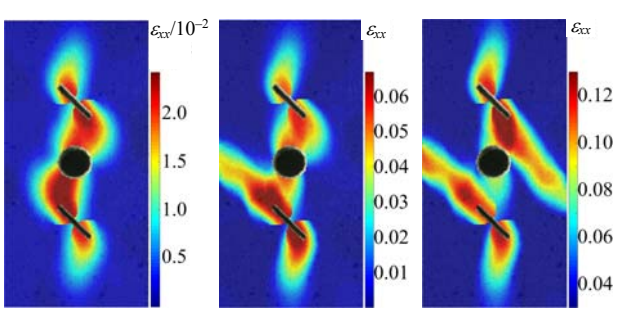

(e) Strain field (point B_0) (f) Strain field (point C_0) (g) Strain field (point D_0)

Fig. 12 Specimen 0-1. (a) Plot of stress versus strain, plus the effective variance. (b–d) Propagation of cracks. (e–g) Snapshots of the strain field.

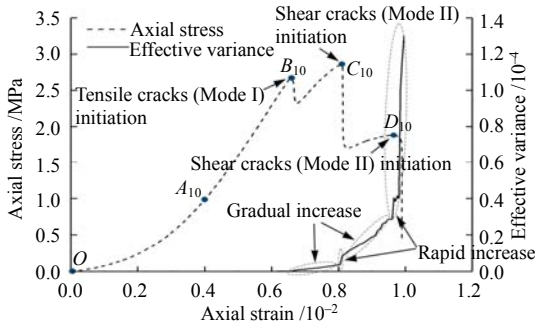

(a) Stress–strain curve

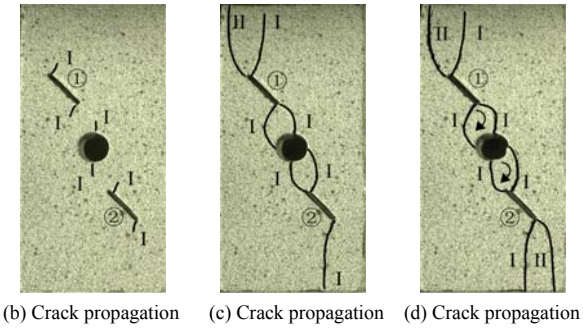

(b) Crack propagation (point B_{10}) (c) Crack propagation (point C_{10}) (d) Crack propagation (point D_{10})

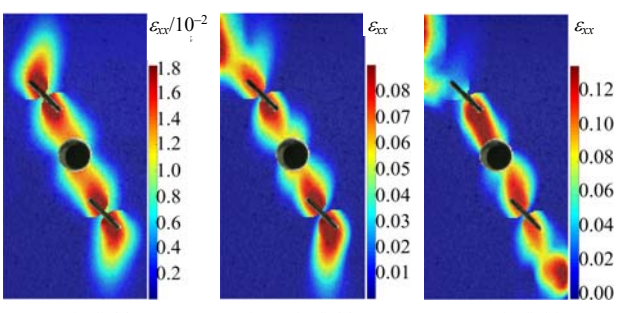

(e) Strain field (point B_{10}) (f) Strain field (point C_{10}) (g) Strain field (point D_{10})

Fig. 13 Specimen 10-1. (a) Plot of stress versus strain, plus the effective variance. (b–d) Propagation of cracks. (e–g) Snapshots of the strain field.

left corner of the specimen and the corresponding strain localization band also propagates to this position, so that the effective variance increases abruptly. At the mark point D_{10}, the shear crack at the tip of the prefabricated crack 2 and the corresponding strain localization band propagate to the lower right corner of the specimen quickly, so that the effective variance increases abruptly again.

(3) Figure 14 shows the stress–strain curve, effective variance, crack propagation and horizontal strain field of the specimen 20-1 when $L=20$ mm. At the mark point B_{20}, a mixed tensile–shear crack (Mode I-II) and the corresponding strain localization band appear suddenly, which connect the hole and the prefabricated cracks. The deviation of the strain measurements increases significantly, so that the effective variance increases rapidly. At the peak stress (the mark point C_{20}), the specimen loses its capacity and slides along the fracture plane, so that the effective variance increases abruptly again.

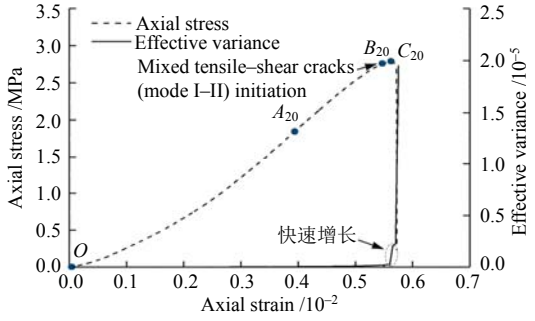

(a) Stress–strain curve

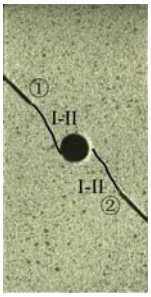

(b) Crack propagation (point B_{20})

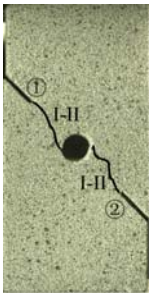

(c) Crack propagation (point C_{20})

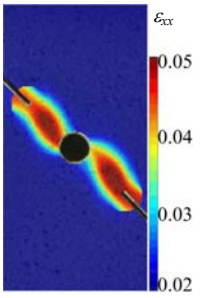

(d) Strain field (point B_{20})

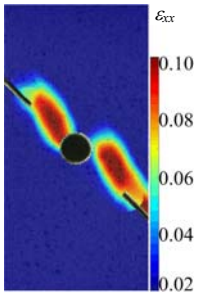

(e) Strain field (point C_{20})

Fig. 14 Specimen 20-1. (a) Plot of stress versus strain, plus the effective variance. (b–c) Propagation of cracks. (d–e) Snapshots of the strain field.

4.4 Identification method of crack type and its mechanism

The dispersion of the strain field is closely related to the development of strain localization band. The initiation and propagation of macroscopic cracks lead to the development of the strain localization band. Our study finds that there is a relation between the variation of the effective variance of the strain field and the crack types of the specimen during the loading process. Therefore, we propose a method for identifying the crack types based on the growth rate of effective variance.

The growth rate of the effective variance (k) at the crack initiatation is defined as

$$k=\frac{V_{e,i+1}-V_{e,i}}{\Delta\varepsilon} \tag{7}$$

where $V_{e,i}$ and $V_{e,i+1}$ are the effective variances at the time of the crack initiation and at the next time step, respectively; and $\Delta\varepsilon$ is the increment of axial strain per time step.

It is worth noting that by checking the video of crack propagation during the uniaxial compression tests, we find that for specimens with $L=0$ mm and $L=10$ mm, the initiation of shear cracks occurs when the tensile cracks stop propagating for a period of time; whereas for specimens with $L=20$ mm, only one crack type occurs, i.e. mixed tensile–shear crack (Mode I-II). Therefore, the variation of the effective variance of the strain field is caused by the initiation and propagation of a single type of crack. The calculation results of the specimens each of which contains a single hole and double cracks are listed in Table 4. It shows that the growth rate of effective variance for the tensile cracks (Mode I) is the smallest, followed by the mixed tensile–shear crack (Mode I-II), and that of the shear cracks (Mode II) is the largest. This is due to the fact that different motion states of the meso-particles appear on both sides of the new crack. The crack propagation is closely related to the direction and magnitude of the meso-particle displacement vector. Therefore, in this study, we use the displacement vector to explain the changes and differences in the growth rate of effective variance from the perspective of meso-mechanics.

Table 4 Growth rate of effective variance

Type of cracks	Growth rate of effective variance /10^{-2}
Mode I	0.72–1.89
Mode II	9.63–32.40
Mode I-II	2.34–3.59

(1) For tensile cracks (Mode I), the meso-particles on both sides of the crack move away from each other at a certain angle. The displacements of meso-particles on both sides are almost equivalent. The meso-particles move at a low speed (see the distributions of displacement vector around the crack Mode I as shown in Figs.10(a) and 10(b)). Therefore, the tensile crack propagates steadily, as shown in Fig.15(a). The development of the corresponding strain localization band and the dispersion of the strain is stable, so that

the effective variance increases constantly, i.e. the growth rate of effective variance is relatively small.

(2) For shear cracks (Mode II), the meso-particles on both sides of cracks move in the same direction along the crack. The displacement of the particles on both sides varies greatly. The meso-particles on one side move fast, whereas on the other side the particles hardly move, resulting in a relative shear motion (see the distributions of displacement vector around the crack Mode II as shown in Fig.10(a) and 10(b)). Therefore, the shear crack appears, as shown in Fig.15(b). The initiation and propagation of shear cracks lead to the rapid development of strain localization bands and the increase of the deviation of the strain field. The growth rate of effective variance increases significantly.

(3) For mixed tensile–shear cracks (Mode I-II), the meso-particles on both sides of cracks move in the opposite direction. The displacement of the particles on one side is significantly larger than that on the other side (see the distributions of displacement vector around the crack Mode I-II as shown in Fig.10(c)). Therefore, the mixed tensile–shear crack appears, as shown in Fig.15(c). However, compared to that of tensile crack, the particles on the both sides of mixed tensile–shear crack move at a smaller angle and show a smaller tensile crack. Compared to that of shear crack, the difference of displacements of the particles on both sides of mixed tensile–shear crack is also smaller, and therefore shows a smaller shear crack. Thus, after the mixed tensile–shear crack appears, the deviation of the strain field is greater than that of tensile cracks and smaller than that of shear cracks. The growth rate of effective variance is between those of the double crack types.

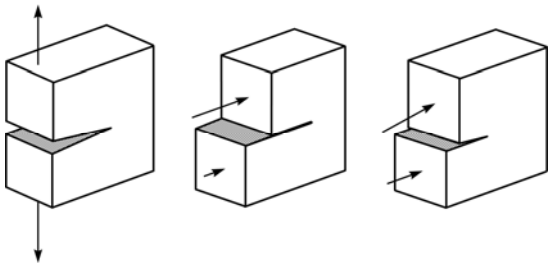

(a) Mode I crack (b) Mode II crack (c) Mode I-II crack

Fig. 15 Three basic types of cracks

In summary, the initiation and propagation of different types of cracks lead to different trends of effective variance. Therefore, the types of cracks can be identified according to the growth rates of effective variance. The cracks can be identified as tensile crack, mixed tensile–shear crack, and shear crack, when the growth rate of effective variance (k) falls into the ranges of 0.72×10^{-2}–1.89×10^{-2}, 2.34×10^{-2}–3.59×10^{-2}, and 9.63×10^{-2}–32.40×10^{-2}, respectively. It needs to be pointed out that our study is only focused on the specimens each of which contains a single hole and double cracks. Further experiments on the rocks containing various kinds of defects with different geometric characteristics are still needed to generalize the conclusion.

5 Conclusions

(1) The material composition and mechanical properties of the 3D sand printed specimens are highly similar to those of natural sandstones. The coefficient of variation of their mechanical properties is less than 0.051 and the ratio of compressive to tensile strength is 12.24:1.00, showing high brittleness and good stability in mechanical properties. Therefore, they can be considered as a rock-like material in rock mechanics experiments. We use 3D sand printing technique to prepare rock specimens each of which contains a single hole and double cracks. Through the uniaxial compression test, we find that the mechanical properties of the specimens are degraded due to the inclusion of the defects. The compressive strength and elastic modulus are reduced by 8.04%–38.91% and 14.44%–27.78%, respectively, compared with those of the specimens each of which merely contains a single hole.

(2) We use the DIC method to monitor the change of strain fields of the specimens during the compression process. It is demonstrated quantitatively that the patterns of crack propagation are influenced by the prefabricated cracks. In combination with the displacement vector method, the crack propagation mechanism is quantitatively revealed from the perspective of meso-mechanics. Based on different motion states of the meso-particles on both sides of the prefabricated crack, three basic types of cracks have been identified successfully, which are tensile crack (Mode I), shear crack (Mode II), and mixed tensile–shear crack (Mode I-II). All the specimens each of which contains a single hole and double cracks show mixed tensile–shear failure (Mode I-II). As the horizontal distance (L) between the hole and the crack increases, the coalescence patterns change from tensile coalescence ($L=0$ mm) to rotation coalescence ($L=$ 10 mm), showing mixed tensile–shear coalescence ($L=$ 20 mm) eventually.

(3) The covariance matrix of three strain components, including horizontal, vertical and shear strains, is calculated. The effective variance of strain field is introduced to quantitatively analyzing the development of the strain field. The results show that the effective variance of strain field changes in different manners after different types of cracks initiate. The growth rate of effective variance of tensile cracks (Mode I) is the smallest, followed by mixed tensile–shear crack (Mode I-II), and that of shear cracks (Mode II) is the largest. Based on the ranges of the growth rate of effective variance, we propose a method to identify the type of cracks, which provides a new perspective for further understanding the failure behaviors of rock containing a single hole and double cracks.

References

[1] LAJTAI E Z, LAJTAI V N. The collapse of cavities[J]. International Journal of Rock Mechanics and Mining Sciences and Geomechanics Abstracts, 1975, 12(4): 81–86.

[2] DU Ming-rui, JING Hong-wen, SU Hai-jian, et al. Experimental study of strength and failure characteristics of sandstone containing prefabricated elliptical hole[J]. Journal of China University of Mining and Technology, 2016, 45(6): 1164–1171.

[3] LI Chong-jin, LI Xi-bing, LI Di-yuan. Particle flow analysis of fracture characteristics of marble with a single hole[J]. Chinese Journal of Engineering, 2017, 39(12): 1791–1801.

[4] HUANG Y H, YANG S Q, MATTHEW R H, et al. Experimental study on uniaxial mechanical properties and crack propagation in sandstone containing a single oval cavity[J]. Archives of Civil and Mechanical Engineering, 2018, 18: 1–15.

[5] ZHU Quan-qi, LI Di-yuan, LI Xi-bing. Experimental study on failure and mechanical characteristics of marble containing a prefabricated elliptical hole[J]. Chinese Journal of Rock Mechanics and Engineering, 2019, 38(Suppl.1): 2724–2733.

[6] WONG R H C, LIN P. Numerical study of stress distribution and crack coalescence mechanisms of a solid containing multiple holes[J]. International Journal of Rock Mechanics and Mining Sciences, 2015(79): 41–54.

[7] LIN P, WONG R H C, TANG C A. Experimental study of coalescence mechanisms and failure under uniaxial compression of granite containing multiple holes[J]. International Journal of Rock Mechanics and Mining Sciences, 2015(77): 313–327.

[8] YANG Sheng-qi, LI Xiang-ru, LI Yu-shou. Experimental analysis of mechanical behavior of sandstone containing hole and fissure under uniaxial compression[J]. Chinese Journal of Rock Mechanics and Engineering, 2012, 31(Suppl.2): 3539–3546.

[9] ZHOU Jun-hua, YANG Kun, FANG Kai, et al. Effect of fissure on mechanical and damage evolution characteristics of sandstone containing hole defect[J]. Journal of Central South University (Science and Technology), 2019, 50(4): 968–975.

[10] WU Tian-hua, ZHOU Yu, WANG Li, et al. Mesoscopic study of interaction mechanism between circular hole and fissures in rock under uniaxial compression[J]. Rock and Soil Mechanics, 2018, 39(Suppl.2): 463–472.

[11] JU Yang, XIE He-ping, ZHENG Ze-min, et al. Visualization of the complex structure and stress field inside rock by means of 3D printing technology[J]. Chinese Science Bulletin, 2014, 59(32): 3109–3119.

[12] JIANG C, ZHAO G. A preliminary study of 3D printing on rock mechanics[J]. Rock Mechanics and Rock Engineering, 2015, 48(3): 1041–1050.

[13] JIANG Q, FENG X T, GONG Y H, et al. Reverse modelling of natural rock joints using 3D scanning and 3D printing[J]. Computers and Geotechnics, 2016, 73(3): 210–220.

[14] ZHOU T, ZHU J B. Identification of a suitable 3D printing material for mimicking brittle and hard rocks and its brittleness enhancements[J]. Rock Mechanics and Rock Engineering, 2018, 51: 765–777.

[15] JIANG Quan, SONG Lei-bo. Application and prospect of 3D printing technology to physical modeling in rock mechanics[J]. Chinese Journal of Rock Mechanics and Engineering, 2018, 37(1): 23–37.

[16] WANG Pei-tao, HUANG Zheng-jun, REN Fen-hua, et al. Investigation of direct shear behavior and fracture patterns of 3D-printed complex jointed models[J]. Rock and Soil Mechanics, 2020, 41(1): 46–56.

[17] ZHANG Ke, QI Fei-fei, CHEN Yu-long. Deformation and fracturing characteristics of fracture network model and influence of filling based on 3D printing and DIC technologies[J]. Rock and Soil Mechanics, 2020, 41(8): 2555–2563.

[18] JIN Ai-bing, WANG Shu-liang, WANG Ben-xin, et al. Study on the fracture mechanism of 3D-printed-joint specimens based on DIC technology[J]. Rock and Soil Mechanics, 2020, 41(10): 3214–3224.

[19] ZHAO Cheng, TIAN Jia-shen, SONG Tian-hao, et al. Crack propagation and damage of rock under uniaxial compression based on global strain field analysis[J]. Chinese Journal of Rock Mechanics and Engineering, 2015, 34(4): 763–769.

[20] ZHOU Cui-ying, LIANG Ning, LIU Zhen. Fractal characteristics of compression failure of red soft rock and cascading failure process[J]. Rock and Soil Mechanics, 2019, 40(Suppl.1): 21–31.

[21] SONG Yi-min, XING Tong-zhen, DENG Lin-lin, et al. Experimental study of evolution characteristics of rock deformation field at different loading rates[J]. Rock and Soil Mechanics, 2017, 38(10): 2773–2779, 2788.

[22] ZHANG Ke, LI Na, CHEN Yu-long, et al. Evolution characteristics of strain field and infrared radiation temperature field during deformation and rupture process of fractured sandstone[J]. Rock and Soil Mechanics, 2020, 41(Suppl.1): 95–105.

[23] JIN Ai-bing, WANG Shu-liang, WANG Ben-xin, et al. Study on the fracture mechanism of specimens containing 3D-printed cross joint based on DIC technology[J]. Rock and Soil Mechanics, 2020, 41(12): 1–12.

[24] MA Shao-peng, LIU Shan-jun, ZHAO Yong-hong. Gray correlation of digital images from loaded rock specimen surface to evaluate its damage evolution[J]. Chinese Journal of Rock Mechanics and Engineering, 2006, 25(3): 590–595.

[25] ZHANG Ke, ZHANG Kai. Gray and texture features of strain field for fractured sandstone during failure process[J]. Journal of China Coal Society, 2021, 46(4): 1253–1262.

[26] TIAN Wei, PEI Zhi-ru, HAN Nü. A preliminary research on three-dimensional reconstruction and mechanical characteristics of rock mass based on CT scanning and 3D printing technology[J]. Rock and Soil Mechanics, 2017, 38(8): 2297–2305.

[27] TIAN Wei, WANG Zhen, ZHANG Li, et al. Mechanical properties of 3D printed rock samples subjected to high temperature treatment[J]. Rock and Soil Mechanics, 2020, 41(3): 961–969.

[28] LI Hua-min, LI Hui-gui, SONG Gui-jun, et al. Physical and mechanical properties of coal-bearing strata rock in Shendong Coalfield[J]. Journal of China Coal Society, 2016, 41(11): 2661–2671.

[29] YIN Q, JING H W, SU H J. Investigation on mechanical behavior and crack coalescence of sandstone specimens containing fissure-hole combined flaws under uniaxial compression[J]. Geosciences Journal, 2018, 22: 825–842.

[30] SHARAFISAFA M, SHEN L M, ZHENG Y G, et al. The effect of flaw filling material on the compressive behaviour of 3D printed rock-like discs[J]. International Journal of Rock Mechanics and Mining Sciences, 2019, 117: 105–117.

[31] PAN B. Recent progress in digital image correlation[J]. Experimental Mechanics, 2011, 51(7): 1223–1235.

[32] PAN Hong-yu, GE Di, ZHANG Tian-jun, et al. Influence of strain rate on the rock fracture propagation law[J]. Journal of China Coal Society, 2018, 43(3): 675–683.

[33] YANG S Q, YIN P F, ZHANG Y C, et al. Failure behavior and crack evolution mechanism of a non-persistent jointed rock mass containing a circular hole[J]. International Journal of Rock Mechanics and Mining Sciences, 2019, 114: 101–121.

[34] GAO K, HARRISON J P. Scalar-valued measures of stress dispersion[J]. International Journal of Rock Mechanics and Mining Sciences, 2018, 106: 234–242.